

**A spectroscopic and computational study of Cm<sup>3+</sup> incorporation in lanthanide phosphate rhabdophane (LnPO<sub>4</sub>·0.67H<sub>2</sub>O) and monazite (LnPO<sub>4</sub>)**

Huittinen, N.; Scheinost, A. C.; Ji, Y.; Kowalski, P. M.; Arinicheva, Y.; Wilden, A.;  
Neumeier, S.; Stumpf, T.;

Originally published:

May 2018

**Inorganic Chemistry 57(2018), 6252-6265**

DOI: <https://doi.org/10.1021/acs.inorgchem.8b00095>

Perma-Link to Publication Repository of HZDR:

<https://www.hzdr.de/publications/Publ-26844>

Release of the secondary publication  
on the basis of the German Copyright Law § 38 Section 4.

# **A spectroscopic and computational study of $\text{Cm}^{3+}$ incorporation in lanthanide phosphate rhabdophane ( $\text{LnPO}_4 \times 0.67\text{H}_2\text{O}$ ) and monazite ( $\text{LnPO}_4$ )**

N. Huittinen<sup>a,\*</sup>, A. C. Scheinost<sup>a,b</sup>, Y. Ji<sup>c,d</sup>, P. M. Kowalski<sup>c,d</sup>, Y. Arinicheva<sup>c,d</sup>, A. Wilden<sup>c,d</sup>, S. Neumeier<sup>c,d</sup>, T. Stumpf<sup>a</sup>

<sup>a</sup>Helmholtz-Zentrum Dresden - Rossendorf, Institute of Resource Ecology, Bautzner Landstraße 400, 01328 Dresden, Germany

<sup>b</sup>The Rossendorf Beamline, The European Synchrotron Radiation Facility (ESRF), P.O. Box 40220, F-38043, Grenoble, France

<sup>c</sup>Forschungszentrum Jülich GmbH, Institute of Energy and Climate Research, Nuclear Waste Management and Reactor Safety (IEK-6), 52425 Jülich, Germany

<sup>d</sup>JARA High-Performance Computing, Schinkelstraße 2, 52062 Aachen, Germany

\*Corresponding author :

Nina Huittinen

email : n.huittinen@hzdr.de

phone : +49 351 260 2148

fax : +49 351 260 3553

Keywords:  $\text{Cm}^{3+}$ , incorporation, monazite, rhabdophane, spectroscopy, *ab initio* simulations

## Abstract

This study investigates the incorporation of the minor actinide curium ( $\text{Cm}^{3+}$ ) in a series of synthetic  $\text{La}_{1-x}\text{Gd}_x\text{PO}_4$  ( $x = 0, 0.24, 0.54, 0.83, 1$ ) rhabdophane and monazite solid solutions. Monazites are envisioned as potential immobilization matrices for high-level radioactive wastes. Rhabdophane is expected to form as alteration product of monazite in contact with water under repository conditions and hence may become the solubility controlling phase over time. To obtain information of the incorporation process on the molecular scale and to understand the distribution of the dopant in the synthetic phosphate phases, combined time-resolved laser fluorescence spectroscopy (TRLFS) and X-ray Absorption Fine Structure (XAFS) spectroscopy investigations have been conducted and complemented with *ab initio* atomistic simulations.  $\text{Cm}^{3+}$  is incorporated in the monazite end-members ( $\text{LaPO}_4$  and  $\text{GdPO}_4$ ) on one specific, highly ordered lattice site. The intermediate solid solutions, however, display increasing disorder around the  $\text{Cm}^{3+}$  dopant as a result of random variations in nearest neighbor distances. Despite this local structural disordering, homogenous monazite solid solutions are obtained for all synthesized  $\text{La}_{1-x}\text{Gd}_x\text{PO}_4$  compositions without the formation of dopant clusters that could potentially hamper the performance of the monazite ceramics for the immobilization of minor actinide containing wastes. In hydrated rhabdophane, and especially its La-rich solid solutions,  $\text{Cm}^{3+}$  is preferentially incorporated on non-hydrated lattice sites. This site occupancy is not in agreement with the hydrated rhabdophane structure, where two thirds of the lattice sites are associated with water of hydration ( $\text{LnPO}_4 \times 0.67\text{H}_2\text{O}$ ), implying that structural substitution reactions cannot be predicted based on the structure of the host matrix only. In addition, slight dehydration of  $\text{GdPO}_4 \times 0.67\text{H}_2\text{O}$  results in the formation of a third, non-equivalent  $\text{Cm}^{3+}$  species within the solid structure, which is not accounted for in the other rhabdophane compositions.

## 1 Introduction

The safe disposal of high-level radioactive wastes (HLW) originating from various sources such as nuclear power plants, reprocessing facilities, or dismantled nuclear weapons will require durable matrices for their immobilization over long time periods. Especially for the immobilization of specific waste streams containing minor actinides ( $\text{Cm}^{3+}$ ,  $\text{Am}^{3+}$ ) or plutonium ( $\text{Pu}^{3+,4+}$ ), crystalline ceramic materials have been envisioned as host matrices due to their high radiation tolerance<sup>1-3</sup>, high dopant loading<sup>4-6</sup>, and chemical durability<sup>5-10</sup>. Such ceramics include lanthanide phosphates ( $\text{LnPO}_4$ ) crystallizing in the monazite structure, which have been shown to incorporate varying compositions of several trivalent actinide and lanthanide elements in well-defined atomic positions within the crystal lattice.<sup>11-15</sup> Furthermore, in coupled substitution reactions, preserving charge neutrality within the ceramic structure, incorporation of ions with differing oxidation states takes place, extending the range of radionuclides present in the HLW that could be incorporated within the monazite matrix.<sup>16-19</sup> The existence of very old natural analogues containing high concentrations of uranium and thorium show that the crystalline phosphate structure is very tolerant towards self-irradiation damages as well as chemical weathering.<sup>3,7,20-21</sup> This high radiation tolerance and low solubility in aqueous media, have been further demonstrated in several studies using both pristine monazites<sup>8,22</sup> as well as monazites co-doped with various inactive lanthanide analogues or actinide elements<sup>23-25</sup>, speaking for their use as host materials for the immobilization of HLW.

The synthesis of monazite ceramics using conventional aqueous routes, involves the precipitation of lanthanide phosphate rhabdophane ( $\text{LnPO}_4 \times 0.67\text{H}_2\text{O}$ ), followed by sintering of this precursor phase to obtain the crystalline ceramic material. Thus, it can be assumed, that actinide incorporation within the phosphate solid would first occur at the precipitation of rhabdophane,

implying that the speciation of the actinides within this precursor phase could have an influence on their speciation in the final ceramic product. Actinide incorporation within the rhabdophane structure has further been shown to take place under repository conditions as a result of monazite re-crystallization as rhabdophane-type solids. A study conducted for mixed phosphate ceramics ( $\beta\text{-Th}_{2.4}\text{U}_{1.6}(\text{PO}_4)_4\text{P}_2\text{O}_7/\text{La}_{0.4}\text{Ce}_{0.4}\text{Gd}_{0.2}\text{PO}_4$ ) showed that dissolved trivalent elements from the ceramic matrix were rapidly re-precipitated as rhabdophane-type solids independent of the initial ceramic composition.<sup>23</sup> Despite the role of rhabdophane as a monazite precursor and as a potential solubility-limiting solid phase under nuclear waste storage conditions, very little is known about actinide incorporation within this solid structure. A few studies report on precipitation of e.g. minor actinides and plutonium as rhabdophane-like phases<sup>26–28</sup>, however, refined crystal structures of these hydrous actinide bearing phosphate compounds remain unknown so far. According to a recent re-examination of the rhabdophane crystal structure<sup>29,30</sup>, there are three distinct rhabdophane structures with different hydration states depending on the synthesis conditions: monoclinic hydrated  $\text{LnPO}_4 \times 0.67 \text{ H}_2\text{O}$ , monoclinic hemihydrated  $\text{LnPO}_4 \times 0.5 \text{ H}_2\text{O}$ , and hexagonal anhydrous  $\text{LnPO}_4$  rhabdophane phases. The crystal structure of the low temperature hydrated monoclinic rhabdophane phase is more complex than the monazite one, in which all lanthanide cations are connected to nine oxygen atoms from coordinating phosphate groups. The lattice of the monoclinic  $\text{LnPO}_4 \times 0.67 \text{ H}_2\text{O}$  phase, on the other hand, could accommodate the actinide dopant on two distinct low symmetry sites: a 9-coordinated site amounting to two thirds (2/3) of the total number of lanthanide sites in the solid structure, where one coordinating oxygen atom originates from a water molecule, and an 8-fold coordinated site (1/3 of available Ln sites) where all oxygen atoms are provided by phosphate groups. The actual population of these two lattice sites by actinide dopants, however, is currently not understood. Thus, for a sound understanding of the long-term performance of monazites as immobilization

matrices especially for trivalent dopants ( $\text{Am}^{3+}$ ,  $\text{Cm}^{3+}$ ,  $\text{Pu}^{3+}$ ), knowledge of the fate of actinides within the solid monazite ceramic should be complemented with a detailed understanding of their uptake within rhabdophane-type secondary phases.

In the present study we have combined two spectroscopic methods, time-resolved laser fluorescence spectroscopy (TRLFS) and extended x-ray absorption fine structure spectroscopy (XAFS) to investigate the incorporation of the minor actinide  $\text{Cm}^{3+}$  in a series of  $\text{La}_{1-x}\text{Gd}_x\text{PO}_4$  monazite solid solutions. These mixed (La,Gd) $\text{PO}_4$  monazites provide excellent conditions for investigating the flexibility of the monazite structure toward differently sized cations ( $r_{\text{La(III)}}^{\text{IX}} = 1.216 \text{ \AA}^{31}$ ,  $r_{\text{Cm(III)}}^{\text{IX}} = 1.146 \text{ \AA}^{32}$ , and  $r_{\text{Gd(III)}}^{\text{IX}} = 1.107 \text{ \AA}^{31}$ ), and the homogeneity of the synthetic solid solutions. In addition, for the first time actinide ( $\text{Cm}^{3+}$ ) incorporation in the rhabdophane phase has been studied on a molecular level using TRLFS. To explain the spectroscopically observed substitution of  $\text{Cm}^{3+}$  for the various site types in the investigated  $\text{La}_{1-x}\text{Gd}_x\text{PO}_4$  monazite and rhabdophane solid solution matrices, we computed the structural arrangements, energetics, and  $\text{MPO}_4$  formula unit volumes of  $\text{Cm}^{3+}$  incorporation using density functional theory-based *ab initio* calculations. Due to slightly different experimental and computational approaches used in the investigations of monazites vs. rhabdophane solids, results and discussion on  $\text{Cm}^{3+}$  incorporation in these two different phases will be presented separately in the following text.

## 2 Materials and methods

### 2.1 Materials synthesis and characterization

Caution!  $^{248}\text{Cm}$  is a radionuclide with a half-life of  $3.48 \times 10^5$  years, decaying through  $\alpha$ -emission (92%) and spontaneous fission (8%). The use of  $^{248}\text{Cm}$  requires the appropriate infrastructure and personnel trained in the handling of alpha-emitting isotopes.

$\text{Cm}^{3+}$ -doped  $\text{La}_{1-x}\text{Gd}_x\text{PO}_4$  ( $x = 0.0, 0.24, 0.54, 0.83, 1.0$ ) rhabdophane and monazite solid solutions were synthesized by precipitation according to the procedure described in our previous study.<sup>15</sup> Lanthanum and gadolinium nitrate salts were dissolved in deionized water in desired relative concentrations. A small aliquot of a  $10^{-4}$  M  $^{248}\text{Cm}^{3+}$  stock solution was pipetted to the solution, followed by slow addition of  $\text{H}_3\text{PO}_4$ , causing precipitation of  $\text{La}_{1-x}\text{Gd}_x\text{PO}_4 \cdot 0.67 \text{ H}_2\text{O}$  rhabdophane doped with approximately 50 ppm  $\text{Cm}^{3+}$ . The rhabdophane-suspension was kept at  $90^\circ\text{C}$  for 1 week to complete the precipitation and allow for better crystallization of the solid phase. Subsequent, the solid was recovered and repeatedly washed with MilliQ water to remove nitrate ions, followed by drying at  $90^\circ\text{C}$  for 12 h and milling in an agate mortar. Part of the obtained rhabdophane material was further calcined for 2 h at  $600^\circ\text{C}$  to remove any nitrate residues, followed by sintering at  $1450^\circ\text{C}$  for 5 h to finally obtain the crystalline monazite ceramic. The actual, obtained composition of the synthetic rhabdophanes and monazites was investigated using SEM-EDX (FEI Quanta 200 FEG scanning electron microscope equipped with Genesis EDS energy dispersive X-ray system). The phase purity, crystallinity, and formation of the solid solutions were characterized using X-ray powder diffraction (PXRD) (D4 Endeavor diffractometer with a  $\theta$ - $2\theta$ -geometry, Bruker AXS GmbH). PXRD patterns were recorded at room temperature in the  $10^\circ \leq 2\theta \leq 130^\circ$  range with a step size of  $\theta(2\theta) = 0.02^\circ$  and a counting time of 2 s per step using  $\text{Cu K}_{\lambda 1,2}$  radiation ( $\lambda = 1.54184 \text{ \AA}$ ) in a domed sample holder for

radioactive samples. Lattice parameters and lattice distortions were determined with the Topas software (Bruker AXS GmbH). All spectroscopic investigations were conducted on the same set of synthetic samples allowing for direct comparison of obtained results without differences in the solid solution compositions.

## 2.2 Spectroscopic investigations of $\text{Cm}^{3+}$ -doped rhabdophane and monazite

### 2.2.1 Time-resolved laser fluorescence spectroscopy (TRLFS)

The characteristic optical spectra of the  $\text{Cm}^{3+}$  cation originate from  $f$ - $f$  transitions between the emitting excited state  ${}^6\text{D}_{7/2}$  (typically denoted with the letter A) and the ground state  ${}^8\text{S}_{7/2}$  (denoted with the letter Z). The excited A-state of the curium ion undergoes crystal field splitting of about  $300\text{-}600\text{ cm}^{-1}$  due to ligand interactions, giving rise to a maximum of four crystal field states  $\text{A}_1\text{-A}_4$  (hot bands).<sup>33</sup> The magnitude of this crystal field splitting influences the  ${}^6\text{D}_{7/2} \rightarrow {}^8\text{S}_{7/2}$  transition energy, usually causing a red-shift of the  $\text{Cm}^{3+}$  emission spectrum to lower energies with increasing ligand field strength. This spectral shift can further be used to detect multiple  $\text{Cm}^{3+}$  species in a solid, which have slightly different ligand surroundings and, thus, different emission peak maxima. The crystal field splitting of the  $\text{Cm}^{3+}$  ground state is small in comparison to the excited state, for the most part in the order of  $10\text{-}20\text{ cm}^{-1}$ .<sup>33</sup> The ground-state splitting is sensitive to both strength and symmetry of the crystal field. In all but centrosymmetric crystal-field symmetries the ground state multiplet splits into four Kramers doublets ( $\text{Z}_1\text{-Z}_4$ ). This means, that a full 4-fold splitting of the ground multiplet is to be expected for  $\text{Cm}^{3+}$  incorporation in the monoclinic monazite and rhabdophane phases investigated in the present study.

The  $\text{Cm}^{3+}$  luminescence lifetime,  $\tau$ , has been correlated with the number of coordinating water molecules around the ion in solution through a linear empirical relationship, Equation 1.<sup>34</sup>



$$n(\text{H}_2\text{O}) = 0.65 \times \tau^{-1} (\text{ms}) - 0.88 \quad (1)$$

For an incorporated ion without hydration water molecules in the first coordination sphere and in the absence of other quench processes (e.g. metal-to-metal energy transfer) the expected luminescence lifetime according to Eq. 1 is approximately 750  $\mu\text{s}$ . However, significantly longer lifetimes ( $> 1 \text{ ms}$ ) have been reported for incorporated  $\text{Cm}^{3+}$  species, e.g. 1.1 ms for  $\text{Cm}^{3+}$  in defect fluorite<sup>35</sup>, 1.8 ms for  $\text{Cm}^{3+}$  in vaterite<sup>36</sup>, and up to 4.6 ms for  $\text{Cm}^{3+}$  in calcite<sup>37</sup>. In addition, water of hydration within the solid structure is likely to cause quenching of the  $\text{Cm}^{3+}$  luminescence signal. Thus,  $\text{Cm}^{3+}$  incorporation in rhabdophane ( $\text{LnPO}_4 \times 0.67\text{H}_2\text{O}$ ) is expected to have shorter lifetimes than  $\text{Cm}^{3+}$  incorporation in the fully dehydrated monazite solids. However, the degree of quenching due to water of hydration in relation to hydration water molecules in the first coordination sphere of the  $\text{Cm}^{3+}$  cation is not fully understood, thus, the use of Eq. 1 to predict the number of structural water molecules in the vicinity of the  $\text{Cm}^{3+}$  cation in the rhabdophane solids should be considered approximate.

In this work direct excitation of  $\text{Cm}^{3+}$  from the ground state ( $^8\text{S}_{7/2}$ ) to the emitting excited state ( $^6\text{D}_{7/2}$ ) was performed with a pulsed Nd:YAG (Spectra Physics) pumped dye laser set-up (Radiant Dyes Narrow Scan K). The emitted luminescence emission light was directed into a spectrograph (Shamrock 303i) equipped with a polychromator with 300, 600, and 1200 lines/mm gratings and the emission was monitored with an intensified CCD camera (Andor iStar) 10  $\mu\text{s}$  after the exciting laser pulse in a time window of 10 ms. The laser pulse energy and the exact excitation wavelength were monitored in every measurement with optical power meter (Newport 1918-R) and wavelength meter (High Finesse WS-5), respectively. To achieve the desired spectral resolution the solid samples were cooled to approximately 10 K in a helium refrigerated cryostat.

### 2.2.2 *X-ray absorption spectroscopy (XAS)*

The finely ground Cm-doped monazite powders were placed in sample holders consisting of polyethylene (inner confinement) and Teflon (outer confinement) for x-ray absorption measurements. Cm-L<sub>III</sub> edge (18970 eV) XAFS spectra were collected at ambient temperature at the Rossendorf Beamline (ESRF, Grenoble, France) under dedicated ring operating conditions of 6 GeV and 150 – 200 mA. A flat, meridionally-bent, 140-cm long Rh-coated silicon mirror was used to collimate the x-ray beam into a Si(111) double-crystal monochromator. The monochromatic x-ray beam was thereafter focused onto the sample by a 1.3-m long, Rh-coated, toroidal silicon mirror, achieving a rejection of higher order harmonics by at least four orders of magnitude. Due to the very low Cm<sup>3+</sup> doping of 50 ppm in the monazite samples, the collection of approximately 30 spectra per sample was necessary to achieve a satisfactory quality of data. The measurements were done in fluorescence mode using gas-filled ionization chambers and a high-purity, 13-element Ge detector (Canberra) with a digital spectrometer (XIA XMap). The high noise level and subsequently necessary accumulation of many spectra limited the total number of samples to be analyzed, i.e. of the five synthesized monazite samples only the Cm<sup>3+</sup>-doped LaPO<sub>4</sub>, La<sub>0.46</sub>Gd<sub>0.54</sub>PO<sub>4</sub>, and GdPO<sub>4</sub> compositions were measured. The collected spectra were energy-calibrated using the absorption edge of a simultaneously measured Zr foil (17998 eV) for each sample, and averaged to improve the signal-to-noise ratio using Sixpack<sup>38</sup>. The acquired spectra were analyzed according to a standard procedure on the program WinXAS (version 3.2).<sup>39</sup> EXAFS theoretical fitting was performed both in *k*-space (i.e. EXAFS oscillation spectra) and R-space (i.e. Fourier transforms: FTs). EXAFS theoretical phase and amplitude functions required for the theoretical fitting were calculated by the program code FEFF 8.20<sup>40</sup> based on the structure of La monazite.

### 2.3 Atomistic simulations of $\text{Cm}^{3+}$ incorporation in monazite and rhabdophane

The lattice parameters of  $\text{La}_{1-x}\text{Gd}_x\text{PO}_4$  monazite and  $\text{La}_{1-x}\text{Gd}_x\text{PO}_4 \times 0.67\text{H}_2\text{O}$  rhabdophane solid solutions were investigated by *ab initio* simulations. Furthermore, the bond-length distribution ( $\text{Cm} \cdots \text{O}$ ) in the monazite solid solutions doped with  $\text{Cm}^{3+}$  were investigated and compared to collected spectroscopic data. The calculations were performed with the DFT-based plane-wave Quantum ESPRESSO code<sup>41</sup> on  $\text{La}_{1-x}\text{Gd}_x\text{PO}_4$  monazite and  $\text{La}_{1-x}\text{Gd}_x\text{PO}_4 \times 0.67\text{H}_2\text{O}$  rhabdophane solid solutions represented by supercells consisting 192 atoms. In order to get the converged wavefunctions, we applied 2x2x2 and 1x3x2 Methfessel–Paxton k-points grids.<sup>42</sup> The ionic arrangements of solid solutions were built with the aid of special quasirandom structures<sup>43</sup> using the procedure described in Li et al. (2014)<sup>25</sup> and Huittinen et al. (2017)<sup>15</sup>. We used PBEsol exchange correction functional which was successfully applied to our previous studies of lanthanide-phosphates.<sup>25, 44-45</sup> The plane-wave energy cutoff was 30 Ry.

The set of energies of  $\text{Cm}^{3+}$  incorporated on different hydrated (24 positions) and non-hydrated (8 positions) sites of  $\text{La}_{1-x}\text{Gd}_x\text{PO}_4 \times 0.67 \text{H}_2\text{O}$  rhabdophane ( $x=0, 0.25, 0.5, 0.75, 1$ ) were calculated. The energy of Cm incorporation into the hydrated and non-hydrated configuration was then derived applying the Boltzmann distribution

$$\langle E \rangle = \frac{\sum_{i=1}^M \varepsilon_i e^{-\varepsilon_i/kT}}{\sum_{i=1}^M e^{-\varepsilon_i/kT}} \quad (2)$$

,where  $\varepsilon_i$  are the energies of the different Cm incorporation ionic configurations with respect to the lowest energy structure,  $k$  is the Boltzmann constant, and  $T=363 \text{ K}$  is the synthesis temperature. Having these incorporation energies, the abundances of curium on non-hydrated and hydrated lattice sites were computed assuming the Boltzmann distribution between the two sites. To account for temperature effects on the lattice site occupancy, another set of calculations was

performed for  $T=1200$  K. This high temperature was chosen to obtain an adequate difference between the site occupancies as a function of temperature.

Finally, for a better understanding of the  $\text{Ce}^{3+}$  distribution on the various lattice sites in rhabdophane matrices, the  $\text{MPO}_4$  formula unit volume was calculated based on the optimized rhabdophane structures for pure phase  $\text{LaPO}_4$ ,  $\text{GdPO}_4$ , and  $\text{CePO}_4$  rhabdophane as well as for  $\text{Ce}^{3+}$ -doped  $\text{LaPO}_4 \times 0.67\text{H}_2\text{O}$  and  $\text{GdPO}_4 \times 0.67\text{H}_2\text{O}$ .

### 3 Results

#### 3.1 Materials characterization

SEM-EDX analysis was performed for the  $\text{La}_{1-x}\text{Gd}_x\text{PO}_4$  monazite solid solutions to determine the actual compositions of the synthesized compounds. As the monazites were obtained by direct calcination and sintering of the rhabdophane precursor phases, identical  $\text{La}^{3+}$  and  $\text{Gd}^{3+}$  contents are expected in both materials. The compositions are compiled in Table 1.

*Table 1: Obtained compositions of the synthetic  $\text{La}_{1-x}\text{Gd}_x$ -phosphates.*

x ( $\text{Gd}^{3+}$ )	Actual composition
1	$\text{GdPO}_4$
$0.83 \pm 0.01$	$\text{La}_{0.17}\text{Gd}_{0.83}\text{PO}_4$
$0.54 \pm 0.03$	$\text{La}_{0.46}\text{Gd}_{0.54}\text{PO}_4$
$0.24 \pm 0.01$	$\text{La}_{0.76}\text{Gd}_{0.24}\text{PO}_4$
0	$\text{LaPO}_4$

PXRD-patterns of  $\text{La}_{1-x}\text{Gd}_x\text{PO}_4 \times 0.67\text{H}_2\text{O}$  rhabdophane and  $\text{La}_{1-x}\text{Gd}_x\text{PO}_4$  monazites are presented in Figure 1. No reflections other than those belonging to the hydrated monoclinic rhabdophane or monazite can be seen in the diffractograms, indicating that single-phase rhabdophane and monazite solid solutions are formed during the synthesis. Lattice parameters for the monazite and rhabdophane solids were derived using Rietveld refinement of collected XRD-data. For hydrated  $\text{La}_{1-x}\text{Gd}_x\text{PO}_4$  rhabdophane solid solutions, this is the first time such parameters are reported.

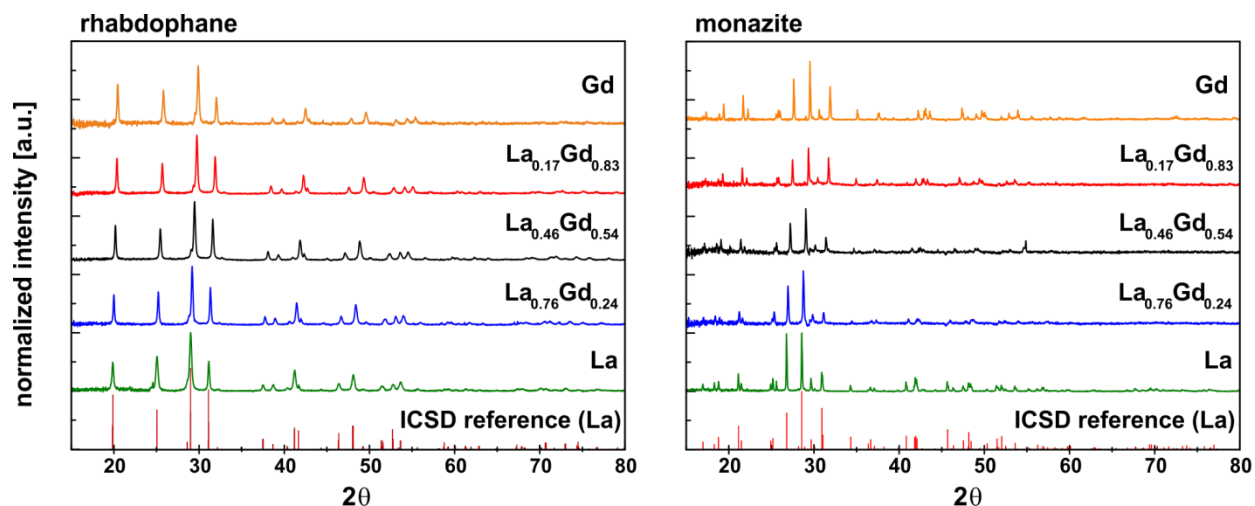


Figure 1: Experimental XRD patterns obtained for the synthetic  $\text{Ce}^{3+}$ -doped  $\text{La}_{1-x}\text{Gd}_x\text{PO}_4$  rhabdophane (left) and monazite (right) phases with the theoretical XRD patterns of the hydrated monoclinic rhabdophane<sup>29</sup> and monazite<sup>46</sup> structures for the La endmember.

Lattice parameters and cell volumes, derived both from experimental PXRD data and *ab initio* calculations, of the rhabdophane and monazite compounds, except for the lattice parameter  $\beta$  of the rhabdophanes, show a linear compositional trend in agreement with Vegard's law, Figure 2. The experimental and computed lattice parameters are in very good concordance with one another. Slightly larger unit cell volumes are obtained computationally for the La-rich rhabdophane and monazite solid solution compositions in comparison to the Rietveld-derived parameters, while the opposite is true for the Gd-heavy solids. The largest difference between experimental and computed data ( $< 1\%$ ) can be seen for the lattice parameter  $\beta$ . For the rhabdophane solid solutions, it deviates from the expected linear behavior according to both DFT calculations and experiment. In the experimental case, this deviation may result from the Rietveld refinement. Here, the reflex broadening due to the relatively low crystallinity of the rhabdophane compounds as well as rather high background due to the contribution of the domed sample holder for radioactive materials could influence the accuracy of the Rietveld refinement results. Another

possibility for the non-linear compositional trend for the lattice parameter  $\beta$ , could be small variations in the hydration state of the hydrated rhabdophane compounds, i.e. water of hydration is slightly lower than the expected 0.67 for fully hydrated, monoclinic rhabdophane. According to literature, a first dehydration step for hydrated rhabdophane has been observed above approximately 80°C.<sup>30,47</sup> In this work, the precipitation of rhabdophane was performed at 90°C for a total duration of 1 week, followed by drying of the solid phase at this temperature for 12 h. Thus, a small amount of dehydration could be expected, leading to a small deviation of the beta angle. The dehydration reaction should be reversible<sup>29,30</sup>, but incomplete rehydration of the compounds cannot be excluded. This is discussed further in connection to the spectroscopic data obtained for the rhabdophane compounds.

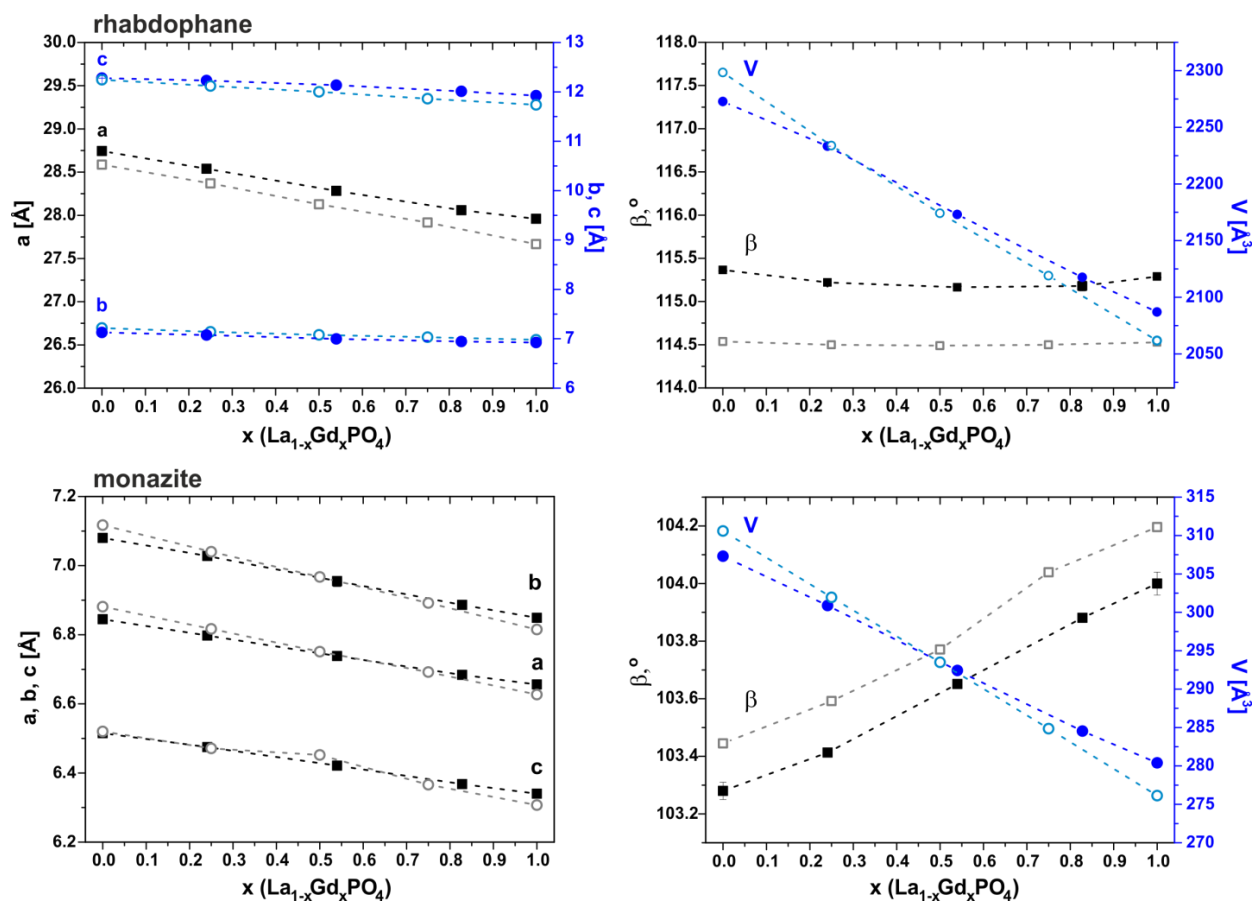


Figure 2: Derived lattice parameters for the synthetic rhabdophane (top) and monazite (bottom) solid solutions. Computed parameters are represented by open symbols and lighter dashed lines than the corresponding experimentally derived data represented by closed symbols.

### 3.2 Spectroscopic investigations of $\text{Cm}^{3+}$ -doped monazites

#### 3.2.1 Time-resolved laser fluorescence spectroscopy

The  $\text{Cm}^{3+}$  excitation spectra obtained with the TRLFS method of the pure  $\text{LaPO}_4$  and  $\text{GdPO}_4$  end-members (Figure 3, left) show four well-resolved peaks corresponding to the 4-fold splitting of the  $\text{Cm}^{3+}$  ground state. The highly resolved ground-state splitting and the absence of additional excitation peaks, indicate the presence of only one, very well-defined, crystalline environment for the incorporated  $\text{Cm}^{3+}$  cation in the La and Gd monazite end-members. The resolved magnitude of the ground-state splitting is approximately  $24 \text{ cm}^{-1}$  for  $\text{GdPO}_4$  and  $27 \text{ cm}^{-1}$  for  $\text{LaPO}_4$ .

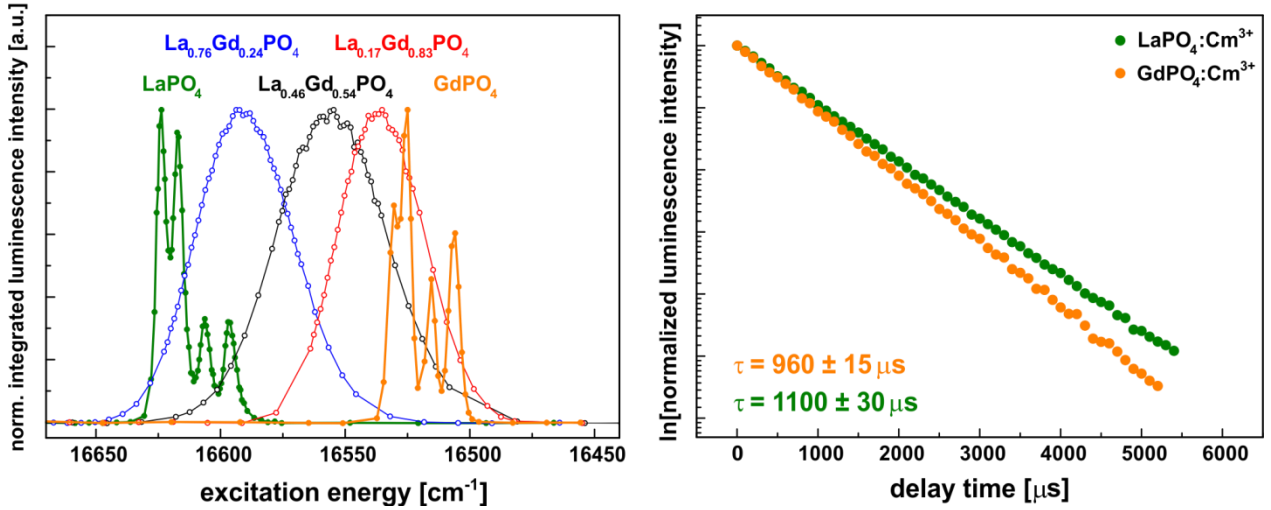


Figure 3: Excitation spectra (left) and selected luminescence lifetimes (right) of the synthetic  $\text{La}_{1-x}\text{Gd}_x\text{PO}_4$  monazite solid solutions doped with 50 ppm  $\text{Cm}^{3+}$ .

The presence of only one  $\text{Cm}^{3+}$  species in the monazite end-member compositions can further be seen in the recorded luminescence lifetimes (Figure 3, right), which decay monoexponentially



with lifetimes of  $1100 \pm 30 \mu\text{s}$  ( $\text{LaPO}_4$ ) and  $960 \pm 15 \mu\text{s}$  ( $\text{GdPO}_4$ ). The long lifetimes speak for a full loss of the  $\text{Ce}^{3+}$  hydration sphere upon incorporation in the monazite lattice, as can be expected after sintering of the samples at  $1450^\circ\text{C}$ .

When examining the  $\text{Ce}^{3+}$  excitation spectra obtained for the solid solution compositions ( $\text{La}_{0.76}\text{Gd}_{0.24}\text{PO}_4$ ,  $\text{La}_{0.46}\text{Gd}_{0.54}\text{PO}_4$ , and  $\text{La}_{0.17}\text{Gd}_{0.83}\text{PO}_4$ ), a complete loss of the splitting fine-structure and a broadening of the excitation peaks can be seen (Figure 3), indicating a decrease of local structural order and formation of randomized solid solutions. When exciting the incorporated  $\text{Ce}^{3+}$  in the solid solution matrix using varying excitation energies, a manifold of narrow emission spectra are obtained, exemplarily shown for the  $\text{La}_{0.46}\text{Gd}_{0.54}\text{PO}_4$  composition in Figure 4.

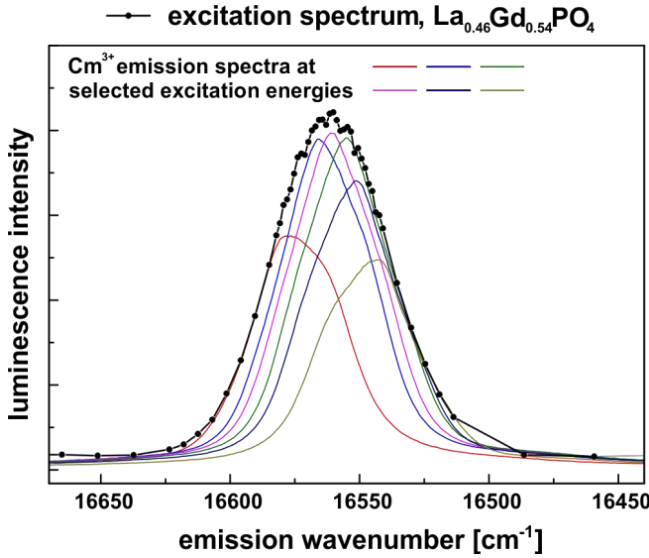


Figure 4: Excitation spectrum of  $\text{Ce}^{3+}$ -doped  $\text{La}_{0.46}\text{Gd}_{0.54}\text{PO}_4$  (black spectrum) and emission spectra showing emission line narrowing collected at various excitation energies (colored spectra).

Such luminescence line narrowing has previously been reported for  $\text{Ce}^{3+}$  adsorption species on the clay mineral kaolinite<sup>48</sup> and for  $\text{Ce}^{3+}$  incorporation in amorphous grain boundaries in bioapatite<sup>49</sup>. In both studies, the observed line narrowing was explained by a continuum of related environments arising from e.g. imperfections on a solid surface or from the lack of long-range order in a solid structure. Thus, in concordance with these studies, the line-narrowing behavior observed in the present study, is attributed to the presence of multiple, very similar local  $\text{Ce}^{3+}$  environments within the monazite solid solution matrix. The origin of this disordering of the solid solution structure will be discussed later in the text.

When plotting the excitation peak position, i.e. the center value of the excitation energy at the full width at tenth maximum (FWTM), for all monazite compositions as a function of  $\text{Gd}^{3+}$  doping (x), a linear trend can be observed (Figure 5). The linear fit of our experimental data yields an expression for the excitation peak maximum given by Equation (3). This allows us to predict the excitation peak maximum for known solid solution compositions or conversely, to calculate the composition of a  $\text{Ce}^{3+}$ -doped  $\text{La}_{1-x}\text{Gd}_x\text{PO}_4$  solid solution from a measured  $\text{Ce}^{3+}$  excitation peak maximum.

$$x_c(^5\text{D}_0 \rightarrow ^7\text{F}_0)[\text{cm}^{-1}] = 16610.7 - 92.6 \cdot x (\text{La}_{1-x}\text{Gd}_x\text{PO}_4) \quad (3)$$

Furthermore, the linear shift of the excitation spectra when going from a larger  $\text{LaPO}_4$  host toward the smaller  $\text{GdPO}_4$  solid implies that the ligand-field exerted on the  $\text{Ce}^{3+}$  cation by the surrounding oxygen ligands becomes systematically stronger, resulting in a bathochromic shift of the excitation spectra. This behavior is in agreement with the decreasing size of the monazite unit cell when going from the larger  $\text{LaPO}_4$  host toward  $\text{GdPO}_4$  and the subsequent contraction of the average  $\text{Ce}\cdots\text{O}$  distance in the solid solutions.

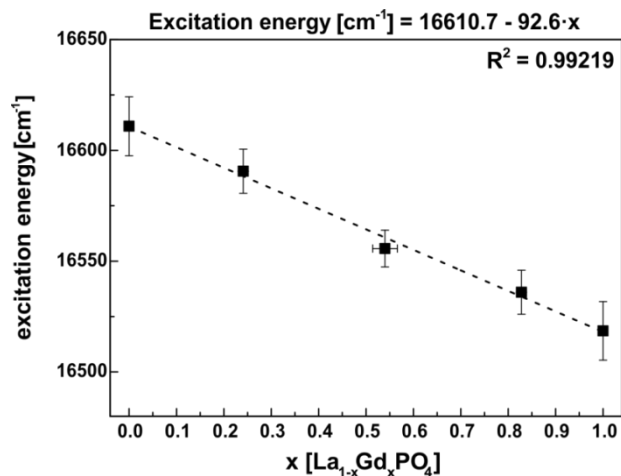


Figure 5: The  $\text{Cm}^{3+}$  excitation peak maxima derived from the excitation spectra in Figure 3 plotted as a function of  $\text{Gd}^{3+}$  substitution ( $x$ ).

### 3.2.2 Extended X-ray absorption spectroscopy

The laser-spectroscopic investigations of the Cm-doped monazite solid solutions were complemented with  $\text{Cm}^{3+}$  L<sub>III</sub>-edge XAFS investigations of the two endmembers and the intermediate solid-solution ( $x = 0.54$ ). The  $k^3$ -weighted EXAFS spectra with corresponding Fourier transform magnitudes (FTs) are presented in Figure 6. The EXAFS signal is dampened by self-absorption effects, and the noise level is high due to the low Cm concentration (50 ppm). Nevertheless, the FTs of all three samples show a backscattering peak at about 2 Å (uncorrected for phase shift), which can be assigned to the Cm-O coordination shell. The fitting of the EXAFS data shows a contraction of the Cm···O distance from 2.46 to 2.43 Å with increasing Gd substitution ( $x$ ) within the  $\text{La}_{1-x}\text{Gd}_x\text{PO}_4$  solid-solution series, Table 2. This is consistent with our laser spectroscopic data presented above and can be explained by the decreasing unit cell and the shortening of Ln···O bond distance, and consequently shorter Cm···O distances, when going from the larger  $\text{LaPO}_4$  monazite toward  $\text{GdPO}_4$ . Furthermore, the Debye-Waller factor (DW,  $\sigma^2$ ) is

smaller for the Cm-O coordination shell of the two endmembers as compared to the solid-solution sample, suggesting a higher structural disorder of the latter one.

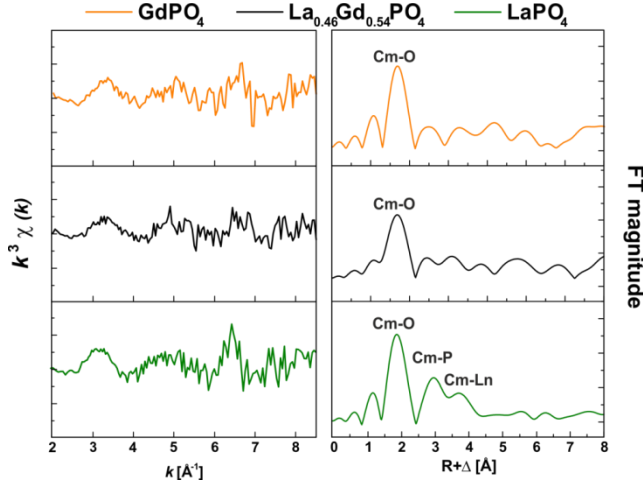


Figure 6: Cm  $L_3$ -edge  $k^3$ -weighted EXAFS spectra (left) and their Fourier transform magnitude (right). Fitted coordination shells are indicated in the figure.

Due to a better signal-to noise ratio in comparison to the other samples, further details of the monazite local structure could be derived for the  $\text{LaPO}_4$  sample (Table 2). The FTs of this sample shows distinct backscattering peaks that can be assigned to Cm-P and Cm-La interactions. In the  $\text{LaPO}_4$  structure, the seven P atoms from the phosphate units directly linked to the  $\text{LaO}_9$  polyhedron have distances ranging from 3.20 to 3.79  $\text{\AA}$ , followed by 3 La neighbors from 4.08 to 4.15  $\text{\AA}$  and another three La neighbors from 4.30 to 4.36  $\text{\AA}$ . By dividing the individual interatomic distances into sub-shells for EXAFS fitting, the Cm-P and Cm-La peaks in the FTs could be described by 3 shorter and 4 longer Cm-P distances and 3 shorter and 3 longer Cm-La distances, respectively. The two Cm-P paths yielded distances at 3.25 and 3.69  $\text{\AA}$ , in line with the  $\text{LaPO}_4$  structure determining the long-range order around  $\text{Cm}^{3+}$ . The two Cm-La shells were fitted with average distances of 4.08 and 4.42  $\text{\AA}$ , again largely in line with the monazite structural model.

Table 2: Fitting results of Cm-L<sub>III</sub> EXAFS data of the Cm-doped monazite solid-solutions (fit range 1.5 – 8.5 Å<sup>-1</sup>). Computed bond lengths, R (cal.), obtained for the DFT optimized monazite structures are included in the table.

Sample	Path	CN	R [Å] (exp.)	R [Å] (cal.)	$\sigma^2$ [Å <sup>2</sup> ]	$\Delta E_0$ [eV]	$S_0^2$	$\chi_{\text{res}}$ [%]
LaPO <sub>4</sub>	Cm-O	9	2.46	2.50	0.0090	7.3	0.80	19.2
	Cm-P	3	3.25	3.33	0.0068 <sup>c</sup>			
	Cm-P	4	3.69	3.72	0.0068 <sup>c</sup>			
	Cm-La	3	4.08	4.14	0.0030 <sup>c</sup>			
	Cm-La	3	4.42	4.36	0.0030 <sup>c</sup>			
La <sub>0.46</sub> Gd <sub>0.54</sub> PO <sub>4</sub>	Cm-O	9	2.43	2.47	0.0120	8.8	0.57	12.6
GdPO <sub>4</sub>	Cm-O	9	2.43	2.46	0.0063	8.8	0.50	16.5

CN: coordination number, error  $\pm 25$  %, R: Radial distance, error  $\pm 0.01$  Å,  $\sigma^2$ : Debye-Waller factor, error  $\pm 0.0005$  Å<sup>2</sup>,  $\Delta E_0$ : phase shift,  $S_0^2$ : amplitude reduction factor,  $\chi_{\text{res}}$ : residual error, c: parameters were correlated during the EXAFS fit.

### 3.3 Atomistic simulations of Cm<sup>3+</sup> incorporation in monazites

In our previous work investigating the incorporation of Eu<sup>3+</sup> in La<sub>1-x</sub>Gd<sub>x</sub>PO<sub>4</sub> monazite solid solutions we could show that the broadening of experimental EXAFS excitation profiles could be explained by an increasing distribution of Eu...O bond lengths in these solid matrices.<sup>15</sup> In the present work, we have performed simulations for Cm<sup>3+</sup> in order to validate such behavior for

actinide-doped monazite solids. The average Cm···O bond lengths simulated for different La<sub>1-x</sub>Gd<sub>x</sub>PO<sub>4</sub> monazite compositions (x= 0, 0.25, 0.5, 0.75, 1) is shown in Figure 7. A linear trend described by Equation 4 is obtained as a function of Gd<sup>3+</sup> substitution (x).

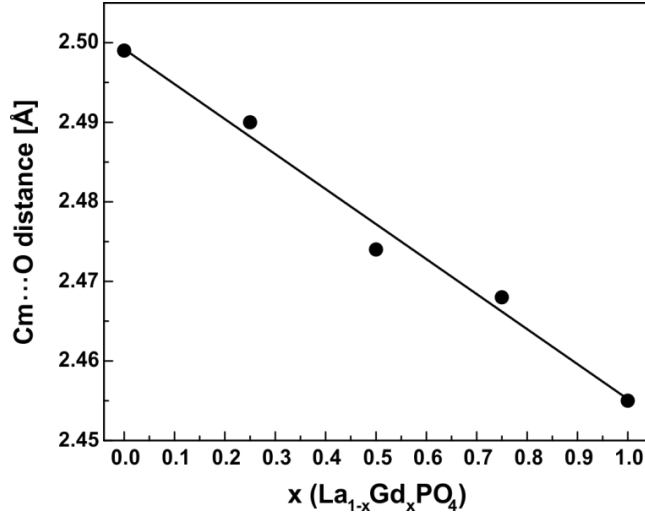


Figure 7: Computed average Cm···O bond lengths in the monazite solid solutions as a function of Gd<sup>3+</sup> fraction, x.

$$\text{Cm} \cdots \text{O} [\text{\AA}] = 2.4992 - 0.044 \cdot x (\text{La}_{1-x}\text{Gd}_x\text{PO}_4) \quad (4)$$

In order to convert the simulated distribution of Cm···O bond lengths in the monazite solid solutions into excitation energies, as done for Eu<sup>3+</sup> in our previous work<sup>15</sup>, Equations 3 and 4 were combined, resulting in a linear expression relating the excitation energy to the Cm···O bond length, Equation 5.

$$E(^5\text{D}_0 \rightarrow ^7\text{F}_0) [\text{cm}^{-1}] = 11351.02 + 2104.545455 \cdot \text{Cm} \cdots \text{O} [\text{\AA}] \quad (5)$$

To allow for direct comparison with experimental TRLFS data, the computed excitation energy profile for the La<sub>0.5</sub>Gd<sub>0.5</sub>PO<sub>4</sub> composition was fitted by Gaussian distribution using Gaussian

normal distribution given by Equation 6, in which  $x_c$  is the excitation peak position and  $\sigma$  is the broadening:

$$f(x) = e^{-\frac{(x-x_c)^2}{2\sigma^2}} \quad (6)$$

As shown in Figure 8, the obtained profile is comparable to the experimental TRLFS spectrum for  $\text{La}_{0.46}\text{Gd}_{0.54}\text{PO}_4$ . The slight blue-shift of the computed profile in comparison to the experimental one may arise from the slightly different solid solution composition with a larger  $\text{La}^{3+}$  content used in the simulations (i.e.  $\text{La}_{0.5}\text{Gd}_{0.5}\text{PO}_4$  instead of  $\text{La}_{0.46}\text{Gd}_{0.54}\text{PO}_4$ ). Similar, broad distributions were obtained for other solid solutions compositions, which indicates that the large broadening of TRLFS profiles for the considered solid solutions is caused by the increasing distribution of  $\text{Cm} \cdots \text{O}$  bond lengths.

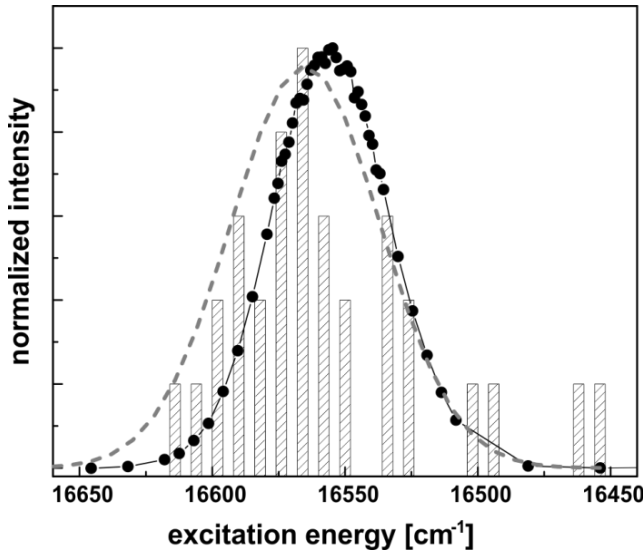


Figure 8: Experimental (solid line) excitation spectrum of the  $\text{La}_{0.46}\text{Gd}_{0.54}\text{PO}_4$  solid solution doped with  $\text{Cm}^{3+}$  and the corresponding Gaussian fitting (dashed line) of the computed distribution (black bars).

Finally, all computed Cm···O bond lengths for the monazite solid solution compositions have been summarized in Table 2, together with the computed Cm···P and Cm···La distances in Cm-doped LaPO<sub>4</sub>, to allow for comparison between experimentally derived (EXAFS) bond lengths. In general, the computed bond lengths are slightly overestimated in comparison to the experimental data. However, the largest difference is below 2.5 % of the experimentally determined value, and the Cm···O bond contraction of 0.04 Å from LaPO<sub>4</sub> to GdPO<sub>4</sub> is in excellent agreement with the experimental value of 0.03 Å. Such small differences between observed and computed bond-lengths are common for application of the DFT method.

### 3.4 Laser spectroscopic investigations of Cm<sup>3+</sup>-doped rhabdophane

The recorded excitation spectra for Cm<sup>3+</sup>-doped LaPO<sub>4</sub> and GdPO<sub>4</sub> rhabdophane compounds are shown in Figure 9, left. Here, also hot-band transitions are shown (denoted with asterisks) as they have been included in the calculations of the relative amounts of various Cm<sup>3+</sup> species in the rhabdophane solids, see discussion later in the text. Two distinct curium species with corresponding hot-bands can be seen for LaPO<sub>4</sub> rhabdophane, while three species exists in GdPO<sub>4</sub>×0.67H<sub>2</sub>O. Especially the curium species found in GdPO<sub>4</sub>×0.67H<sub>2</sub>O are rather ill-defined, yielding asymmetric emission spectra (Figure 9, right) that seem to have two local maxima rather than one clear emission peak. This asymmetry may to some extent arise from the non-resolved ground state splitting of the incorporated Cm<sup>3+</sup> species, but local imperfections around the Cm<sup>3+</sup> cation site or slightly different host lattice environments (see analogy to the monazite solid solutions discussed above) certainly play a role as well. Despite this asymmetry, three clearly distinguishable Cm<sup>3+</sup> species are present in GdPO<sub>4</sub> rhabdophane, two of which are also found in LaPO<sub>4</sub> rhabdophane. For the solid solution compositions (La<sub>0.76</sub>Gd<sub>0.24</sub>PO<sub>4</sub>×0.67H<sub>2</sub>O, La<sub>0.46</sub>Gd<sub>0.54</sub>PO<sub>4</sub>×0.67H<sub>2</sub>O, and La<sub>0.17</sub>Gd<sub>0.83</sub>PO<sub>4</sub>×0.67H<sub>2</sub>O), two species are found, in agreement



with the  $\text{LaPO}_4$  rhabdophane solid, i.e. only  $\text{GdPO}_4$  rhabdophane shows the presence of three curium species.

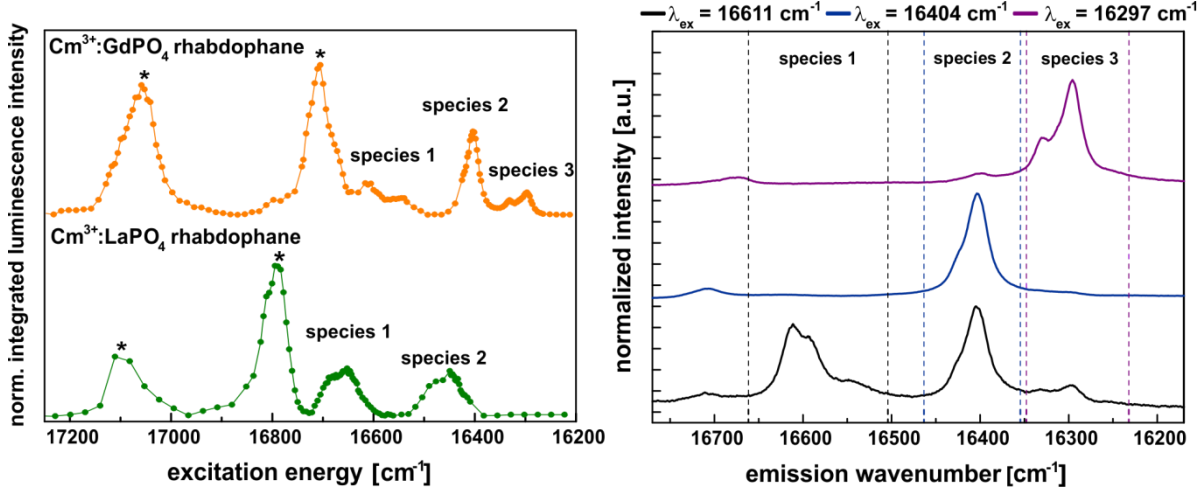


Figure 9: Left – measured excitation spectra of  $\text{Cm}^{3+}$ -doped  $\text{LaPO}_4$  and  $\text{GdPO}_4$  rhabdophane. Hot-band transitions ( $Z_1 \rightarrow A_2/A_3$ ) are denoted with asterisks. Right – emission spectra of the three different  $\text{Cm}^{3+}$  species found in  $\text{GdPO}_4$  rhabdophane. The excitation energies used for the collection of the respective emission spectra are denoted on top of the figure.

By carefully selecting the excitation energy, the various species can be individually excited and both emission spectra and lifetimes can be recorded for the respective species. However, especially for  $\text{GdPO}_4 \times 0.67\text{H}_2\text{O}$  with three  $\text{Cm}^{3+}$  species present within the solid structure, hot-band transitions (typically  $Z_1 \rightarrow A_2$ ) of energetically lower lying species overlap with the main transition ( $Z_1 \rightarrow A_1$ ) of higher-lying species, i.e. a perfect separation of the three species could not be achieved. This is visible in e.g. the emission spectra Figure 9, right, where the bottom (black) spectrum shows the presence of all three species despite “selective” excitation at  $16611 \text{ cm}^{-1}$ , i.e. at the excitation energy maximum of the first  $\text{Cm}^{3+}$  species (species 1). Due to this overlap, the recorded lifetime of this species 1 in  $\text{GdPO}_4$  rhabdophane shows multi-exponential decay behavior (Figure 10), while monoexponential decay curves, corresponding to the lifetimes

of individual  $\text{Cm}^{3+}$  species, are obtained in all other cases for the  $\text{LaPO}_4$  and  $\text{GdPO}_4$  rhabdophane solids.

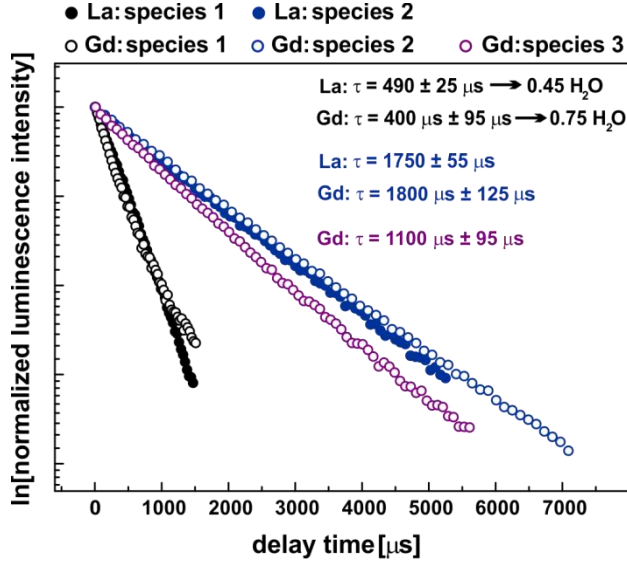


Figure 10: Recorded lifetimes for the individual  $\text{Cm}^{3+}$  species present in  $\text{LaPO}_4 \times 0.67\text{H}_2\text{O}$  (closed symbols) and  $\text{GdPO}_4 \times 0.67\text{H}_2\text{O}$  (open symbols).

The lifetimes obtained for species 1 and species 2 are comparable for  $\text{Cm}^{3+}$  incorporated in  $\text{LaPO}_4 \times 0.67\text{H}_2\text{O}$  and  $\text{GdPO}_4 \times 0.67\text{H}_2\text{O}$ . Species 1 in these solids is characterized by a short lifetime of 400-490  $\mu\text{s}$ , while species 2 is substantially longer, 1750-1800  $\mu\text{s}$ . The third species which is present in  $\text{GdPO}_4 \times 0.67\text{H}_2\text{O}$  only, has a lifetime of  $1100 \pm 95 \mu\text{s}$ . By using Eq. 1 to correlate the recorded lifetimes to the number of hydration water molecules around the  $\text{Cm}^{3+}$  cation,  $n(\text{H}_2\text{O})$  values below zero are obtained for species 2 and species 3, implying that these  $\text{Cm}^{3+}$  species are incorporated within the rhabdophane solids on lattice sites which are not associated with water of hydration or other luminescence quenchers. Species 1 on the other hand yields approximately  $0.45 \pm 0.07 \text{ H}_2\text{O}$  entities for  $\text{Cm}^{3+}$  in  $\text{LaPO}_4 \times 0.67\text{H}_2\text{O}$  and  $0.75 \pm 0.32 \text{ H}_2\text{O}$  for  $\text{Cm}^{3+}$  in  $\text{GdPO}_4 \times 0.67\text{H}_2\text{O}$  when using Eq 1. This would imply that  $\text{Cm}^{3+}$  incorporation has occurred on a lattice site in rhabdophane that is in direct contact with water of hydration. As

previously stated, Eq.1 cannot be used to predict the exact number of hydration water molecules associated with the  $\text{Cm}^{3+}$  lattice site, as the quenching behavior of such water molecules is not fully understood. Based on the refined structure of rhabdophane, however, the lattice site should contain one water of hydration.<sup>29</sup> Further discussion of the various lattice sites in the rhabdophane solids is given in the following section.

### 3.5 Determination of the site occupancy in $\text{Cm}^{3+}$ -doped rhabdophane compounds

The site occupancy of  $\text{Cm}^{3+}$  in the rhabdophane solid solutions has been derived from the experimental TRLFS data presented above, and *ab initio*-based calculations of the lattice site energetics as given by Equation 2.

The experimental  $\text{Cm}^{3+}$  site occupancy in the rhabdophane solid solutions was calculated by relating the magnitude of the TRLFS excitation peak intensities of individual curium species to the total excitation peak intensity of all curium species in the system. Due to the overlap of hot-band transitions (typically  $Z_1 \rightarrow A_2$ ) and main transition ( $Z_1 \rightarrow A_1$ ), as explained above, only the integrated intensity of the lowest-lying species with the largest crystal field splitting could be determined without interference from other species. Thus, in those rhabdophane compositions with only two  $\text{Cm}^{3+}$ -species present, i.e. all solids except  $\text{GdPO}_4 \times 0.67\text{H}_2\text{O}$ , the percentages of the individual species were obtained by integrating the total excitation peak intensity including the hot-bands, and thereafter integrating the total excitation energy of species 2 (without interference of species 1). The presence of three curium species in the  $\text{GdPO}_4$  rhabdophane solid clearly hampered the accurate determination of the site occupancies, where the absolute integrals of especially the minor species (species 1 and species 3, see Figure 9, left) could not be properly separated from the rather dominant signal originating from species 2. Thus, these site

occupancies are connected to rather high uncertainties as seen in Figure 11, left, where the experimentally derived site occupancies are presented as a function of  $\text{Gd}^{3+}$  substitution ( $x$ ).

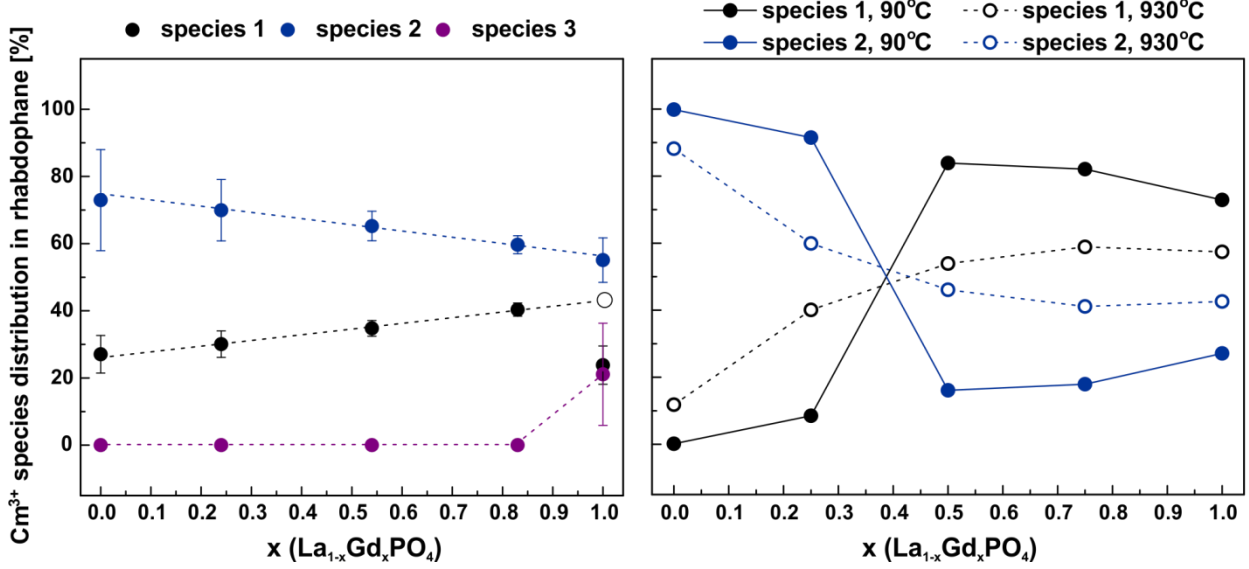


Figure 11: Derived experimental (left) and computational (right)  $\text{Cm}^{3+}$  site occupancies as a function of  $\text{Gd}^{3+}$  substitution ( $x$ ) in the rhabdophane solid solutions. The open blue symbol for the  $\text{GdPO}_4$  rhabdophane composition (left), illustrates the expected percentage of species 1, assuming a linear compositional trend with increasing  $x$ , in the absence of species 3.

The distribution of  $\text{Cm}^{3+}$  between hydrated and non-hydrated cation sites at two different temperatures derived from atomistic simulations is shown in Figure 11, right. The *ab initio* energies show that for La-rhabdophane the non-hydrated site is preferred by 20 kJ/mol, while for Gd-rabdophane the hydrated site is preferred, but only by 3 kJ/mol. We note that although such small energy differences are difficult to be accurately captured by DFT<sup>45</sup> the resulting trend indicates preference for non-hydrated sites in La-rich solutions and approximately equal distribution in Gd-rich compositions, which is well consistent with the experiment. Furthermore, our results imply that higher temperatures promote incorporation of  $\text{Cm}^{3+}$  on non-hydrated sites. We are fully aware that the high temperature (930 °C) used in the simulations, would cause

complete dehydration of rhabdophane under “real” conditions. However, as the purpose of the simulations was to adequately illustrate the influence of temperature on the  $\text{Cm}^{3+}$  site occupancy, chemical changes of the rhabdophane phase itself were not considered.

To understand the incorporation behavior of  $\text{Cm}^{3+}$  in the rhabdophane matrices, we complemented the computational results with calculated volumes per  $\text{MPO}_4$  formula unit ( $M = \text{La, Gd or Cm}$ ) for pure rhabdophane phases and for Cm-doped rhabdophane on hydrated (hyd) and non-hydrated (non-hyd) lattice sites in  $\text{Cm}^{3+}:\text{LaPO}_4 \times 0.67\text{H}_2\text{O}$ ,  $\text{Cm}^{3+}:\text{GdPO}_4 \times 0.67\text{H}_2\text{O}$  and  $\text{CmPO}_4 \times 0.67\text{H}_2\text{O}$ . The volumes of hydrated and non-hydrated Cm species in  $\text{CmPO}_4 \times 0.67\text{H}_2\text{O}$  are derived by comparing volumes of  $\text{CmPO}_4 \times 0.67\text{H}_2\text{O}$  and  $\text{CmPO}_4$  (rhabdophane supercell with all waters removed). The results are compiled in Table 3. When looking at the obtained values, it is clear that non-hydrated Cm species are larger than the hydrated ones and, thus, can be expected to prefer larger host lattice sites. A comprehensive discussion of the site occupancy will be given later in the text.

Table 3: *Computed volumes per  $\text{MPO}_4$  formula unit ( $M = \text{La, Gd, Cm}$ ) for pure rhabdophane phases and for  $\text{Cm}^{3+}$  incorporated on hydrated (hyd) and non-hydrated (non-hyd) lattice sites in  $\text{LaPO}_4 \times 0.67\text{H}_2\text{O}$ ,  $\text{GdPO}_4 \times 0.67\text{H}_2\text{O}$ , and  $\text{CmPO}_4 \times 0.67\text{H}_2\text{O}$ .*

Rhabdophane composition (site type)	Vol/ $\text{MPO}_4$ ( $\text{\AA}^3$ )
$\text{LaPO}_4 \cdot 0.67\text{H}_2\text{O}$	95.761
$\text{GdPO}_4 \cdot 0.67\text{H}_2\text{O}$	85.910
$\text{CmPO}_4 \cdot 0.67\text{H}_2\text{O}$	89.986
$\text{CmPO}_4 \cdot n\text{H}_2\text{O}$ (hyd)	89.031

$\text{CmPO}_4 \cdot 0.67\text{H}_2\text{O}$ (non-hyd)	91.897
$\text{Cm}^{3+}:\text{LaPO}_4 \cdot 0.67\text{H}_2\text{O}$ (hyd)	89.849
$\text{Cm}^{3+}:\text{LaPO}_4 \cdot 0.67\text{H}_2\text{O}$ (non-hyd)	94.503
$\text{Cm}^{3+}:\text{GdPO}_4 \cdot 0.67\text{H}_2\text{O}$ (hyd)	90.389
$\text{Cm}^{3+}:\text{GdPO}_4 \cdot 0.67\text{H}_2\text{O}$ (non-hyd)	89.319

## 4 Discussion

### *Monazites*

The combined data obtained in our laser- and x-ray absorption spectroscopic investigations of the  $\text{Ce}^{3+}$ -doped  $\text{La}_{1-x}\text{Gd}_x\text{PO}_4$  monazite solid solutions clearly show that  $\text{Ce}^{3+}$  is incorporated in all solids on the crystallographic lattice sites within the ceramic structure. The resolved ground-state splitting obtained with the TRLS method for  $\text{Ce}^{3+}$  incorporated in the  $\text{LaPO}_4$  and  $\text{GdPO}_4$  end-members (Figure 3) is a clear indication for a single, very well defined (crystalline) environment in the monazite hosts. For the solid solution compositions ( $\text{La}_{0.76}\text{Gd}_{0.24}\text{PO}_4$ ,  $\text{La}_{0.46}\text{Gd}_{0.54}\text{PO}_4$ , and  $\text{La}_{0.17}\text{Gd}_{0.83}\text{PO}_4$ ), a complete loss of this splitting fine-structure and a broadening of the excitation peaks could be seen, implying a decrease of order in the solids. This is also visible in our XAFS investigations when examining the Debye-Waller factors obtained in the fitting of our EXAFS data, see Table 2. The DW factor is an indicator for thermal and structural disorder and it can be seen to decrease from  $0.0090 \text{ \AA}^2$  in  $\text{LaPO}_4$  to  $0.0063 \text{ \AA}^2$  in  $\text{GdPO}_4$ , while it is substantially larger for the  $\text{La}_{0.46}\text{Gd}_{0.54}\text{PO}_4$  solid-solution composition ( $0.0120 \text{ \AA}^2$ ). The higher structural disorder in the  $\text{LaPO}_4$  end-member in comparison to  $\text{GdPO}_4$  can be understood when examining the cation radii of  $\text{La}^{3+}$ ,  $\text{Ce}^{3+}$ , and  $\text{Gd}^{3+}$ . The dopant vs. host cation radii show a difference of approximately 6% and 3.5 % for  $\text{Ce}^{3+}$  vs.  $\text{La}^{3+}$  and  $\text{Ce}^{3+}$  vs.  $\text{Gd}^{3+}$ , respectively, i.e. a larger mismatch in the larger  $\text{LaPO}_4$  host. This mismatch causes a slightly larger distortion around the  $\text{Ce}^{3+}$  dopant site, which is the probable reason for the larger DW factor obtained for the larger  $\text{LaPO}_4$  host. Such behavior, i.e. a larger disorder in  $\text{LaPO}_4$  than  $\text{GdPO}_4$  monazite, has previously been observed for  $\text{Eu}^{3+}$  incorporation in monazite end-members<sup>50</sup>, where the  ${}^7\text{F}_1$  and  ${}^7\text{F}_2$  emission transitions of the incorporated  $\text{Eu}^{3+}$  cation were used as an indicator for the relative increase or decrease of the site symmetry in the various monazites. The largest  ${}^7\text{F}_2/{}^7\text{F}_1$  ratio (0.50), i.e. the

lowest relative site-symmetry was obtained for  $\text{Eu}^{3+}$  incorporation in the large  $\text{LaPO}_4$  host, while  $\text{Eu}^{3+}$  incorporation in  $\text{GdPO}_4$  monazite yielded the lowest  ${}^7\text{F}_2/{}^7\text{F}_1$  ratio (0.37). In concordance with the present study, this phenomenon was explained by the slight distortion of the crystal lattice accommodating a dopant with a dissimilar cation radius and the subsequent lowering of the site symmetry.

The substantially larger DW factor obtained in the present work for  $\text{La}_{0.46}\text{Gd}_{0.54}\text{PO}_4$  in comparison to the monazite end-members implies a further loss of structural order around the dopant in comparison to the monazite end-members. This is consistent with the observed line-broadening for the solid solution excitation spectra in the TRLFS investigations, Figure 3. In atomistic simulations we could reproduce the line width of the excitation peaks by calculating the  $\text{Ce}\cdots\text{O}$  bond length distribution in the solids solutions and correlating the bond lengths to excitation energies using Equation 5. Thus, both the high DW factor obtained in the XAFS fitting, and the spectral broadening observed with the TRLFS method can be explained by the increasingly broad distribution of possible  $\text{Ce}\cdots\text{O}$  bond lengths in the solid-solution compositions in comparison to the end-members with very well-defined  $\text{Ce}\cdots\text{O}$  distances. The different  $\text{Ce}\cdots\text{O}$  distances are also the cause of the emission line narrowing presented in Figure 4, where the presence of multiple  $\text{Ce}^{3+}$  species differing only in the  $\text{Ce}\cdots\text{O}$  distance, experiencing slightly different ligand field strengths, will give rise to the observed “continuum” of emission peaks for the solid solution compositions.

The systematic bathochromic shift of the  $\text{Ce}^{3+}$  excitation spectra when going from the larger  $\text{LaPO}_4$  host toward the smaller  $\text{GdPO}_4$  monazite has already been explained to occur due to the stronger ligand-field exerted on the  $\text{Ce}^{3+}$  cation by the surrounding oxygen ligands as a function of decreasing size of the monazite unit cell. This is further confirmed by the XAFS fits showing a



contraction of the Cm···O distances (Table 2) from LaPO<sub>4</sub> to GdPO<sub>4</sub>, corroborating our interpretation of the laser spectroscopic data. The bond distances derived in our *ab initio* calculations show a similar trend, however, the overall bond-lengths tend to be slightly longer than the experimentally derived ones (Table 2). Interestingly, the Cm···O bond contraction is much smaller than the overall Ln···O bond contraction derived from the refined monazite structures published in Ni et al.<sup>46</sup>. A decrease of only 0.03 Å (experimental) or 0.04 Å (computed) for Cm···O in LaPO<sub>4</sub> vs. GdPO<sub>4</sub> is observed, while the La···O and Gd···O bonds display a difference of 0.1 Å in the monazite end-members. A similar behavior was obtained in our recent study on plutonium incorporation in LaPO<sub>4</sub> monazite.<sup>51</sup> Here, the Pu···O distance in LaPO<sub>4</sub> remained unchanged at 2.48 Å for doping levels between 1-15%, whereas a decrease of a mere 0.01 Å in pure PuPO<sub>4</sub> (2.47 Å) was observed. This behavior obtained for both Pu and Cm in the monazite hosts implies that the local environments of La and Gd in the host structures are adjusting to accommodate the incorporated actinide cations, rather than the actinide environments adjusting to the size of the LnO<sub>9</sub> polyhedron in the host crystal lattice.

Finally, the systematic trend in the Cm<sup>3+</sup> luminescence behavior as a function of Gd<sup>3+</sup> substitution (x), allows us to exclude Cm<sup>3+</sup> clustering within the solid solutions, as Cm-rich monazite clusters within the solid structure would result in distinctly different excitation peak maxima and a disruption of the linear trend observed for the solid solution compositions. This is again in concordance with our XAFS results, where no Cm-Cm backscatter was detected in the recorded EXAFS spectra. The absence of clustering is of great importance when considering the performance of monazite materials as immobilization matrices for highly radioactive actinide compounds, as a preferential clustering of dopants around matching lattice sites could lead to

incongruent leaching rates and further to an inadequate retention of the radionuclides in a deep geological repository environment.

### *Rhabdophane*

The incorporation of actinides in rhabdophane has been studied for the first time from the perspective of the dopant itself. As expected, the presence of two cation sites (hydrated and non-hydrated) within the hydrated rhabdophane matrix influences the incorporation behavior of the actinide. In contrast to the monazites where only one host cation site is available for  $\text{Cm}^{3+}$  incorporation, our study shows that two or three different actinide species are present in the synthesized rhabdophane solids, depending on composition. Interestingly, the site occupancy derived both experimentally from our TRLFS investigations and computationally by calculating the energy of Cm incorporation into the hydrated and non-hydrated configurations, is not in agreement with the fully hydrated rhabdophane structure. As previously described, two thirds of the sites in hydrated rhabdophane are associated with water of hydration, leaving only one third of the sites non-hydrated. According to experimental data, all rhabdophane compositions show preferential incorporation of  $\text{Cm}^{3+}$  on the non-hydrated site, while *ab initio* calculations result in slightly higher hydrated site occupancies in comparison to the non-hydrated sites for high  $\text{Gd}^{3+}$  substitutions, depending on temperature, Figure 11. However, a 67 % vs. 33% hydrated vs. non-hydrated site occupancy is not obtained in any case. Thus, our study emphasizes the importance of spectroscopic methods to accurately determine site occupancies, which clearly cannot be predicted based on the structure of the host matrix only.

The underlying reason for the site occupancy can be understood when looking at our calculated  $M\text{PO}_4$  formula unit volumes for  $\text{Cm}^{3+}$  incorporation on hydrated and non-hydrated lattice sites in  $\text{LaPO}_4 \times 0.67\text{H}_2\text{O}$  and  $\text{GdPO}_4 \times 0.67\text{H}_2\text{O}$  (Table 3). In  $\text{LaPO}_4$ -rhabdophane, the non-hydrated site is

significantly larger than the hydrated one. When comparing the formula unit volume for pure  $\text{CmPO}_4$  rhabdophane for both hydrated and non-hydrated positions, only the larger non-hydrated site in the La-heavy rhabdophane solids can accommodate both  $\text{Cm}^{3+}$  species without inducing local strain around the dopant cation. This is the likely explanation for the preferential incorporation of  $\text{Cm}^{3+}$  on non-hydrated lattice sites in La-rich rhabdophane compositions. In  $\text{GdPO}_4$  rhabdophane, the situation is different. Here, both sites are too small in comparison to pure  $\text{CmPO}_4$  rhabdophane, implying that a distortion of the lattice is required upon incorporation of  $\text{Cm}^{3+}$ . The resulting  $\text{CmPO}_4$  formula unit volumes in Gd-heavy rhabdophane solids are very similar in size, with a slightly larger volume for the hydrated sites, resulting in a small preference for  $\text{Cm}^{3+}$  incorporation on these site types according to our *ab initio* calculations. Our experimental data deviates slightly from this behavior for the Gd-heavy rhabdophane compositions. In neither of the samples, a preferential incorporation on the hydrated sites is obtained. Instead, the formation of a third species in the pure  $\text{GdPO}_4 \times 0.67\text{H}_2\text{O}$  solid is observed, which is not accounted for in the other synthesized rhabdophane solids. Based on the luminescence lifetime of this species ( $1100 \pm 95 \mu\text{s}$ ), there are no quenching entities, such as water of hydration, directly associated with the incorporated curium cation. This would exclude the presence of small amounts of other low temperature phosphate phases with more water of hydration in the structure, such as churchite/weinschenkite ( $\text{LnPO}_4 \times 2\text{H}_2\text{O}$ ), which under certain experimental conditions could coexist with rhabdophane for Gd to Dy, but not for the larger lanthanides like La.<sup>52</sup> In contrast, it is more likely that slight dehydration of the hydrated rhabdophane structure has occurred for the  $\text{GdPO}_4 \times 0.67\text{H}_2\text{O}$  solid, leading to the presence of another dehydrated site for curium incorporation. In a recent publication by Mesbah et al. (2017)<sup>30</sup>, investigating the stepwise dehydration of rhabdophane, the authors could confirm a first dehydration step with a loss of 0.167 water molecules between 60°C and 140°C, depending on

the size of the host lanthanide, leading to the formation of hemihydrated rhabdophane,  $\text{LnPO}_4 \times 0.5\text{H}_2\text{O}$ . This hemihydrated rhabdophane structure has two cation sites associated with water of hydration and two cation sites that do not coordinate with water. The dehydration temperature was shown to decrease linearly with decreasing cation radius. For La and Gd-rhabdophanes, dehydration temperatures of around 140°C and 60°C, respectively, were found. Thus, bearing in mind that our rhabdophane synthesis was carried out at 90°C, it is indeed likely that dehydration, followed by incomplete rehydration of the Gd-rhabdophane solid has occurred, leading to the presence of additional cation sites for curium incorporation in the examined solid. In addition, when examining the published values for lattice parameters of the fully hydrated and hemihydrated rhabdophane solids, a very small increase (< 0.2 %) of the unit cell volume is observed in the dehydration process, while the  $\beta$  angle increases from 115.23° ( $\text{SmPO}_4 \times 0.667\text{H}_2\text{O}$ )<sup>29</sup> to 133.73° ( $\text{SmPO}_4 \times 0.5\text{H}_2\text{O}$ )<sup>30</sup>. This rather large increase of the  $\beta$  angle could indeed explain the non-linear behavior of this lattice parameter obtained in Rietveld refinement of our rhabdophane PXRD data and serves as a further indication of a slight dehydration of the  $\text{GdPO}_4 \times 0.67\text{H}_2\text{O}$  composition during synthesis.

Finally, according to published data,<sup>29,30</sup> one more rhabdophane dehydration step is expected to occur, leading to the formation of hexagonal dehydrated rhabdophane ( $\text{LnPO}_4$ ), before phase transformation to monazite at temperatures above 1000°C takes place. Thus, multiple coexisting rhabdophane phases, deviating in their degree of hydration, are likely to form under repository conditions in the proximity of the heat-generating waste matrix, further influencing or complicating the actinide incorporation behavior within this mixed “low-temperature” phase.

In the present study, we have for the first time shown that the presence of multiple non-equivalent sites in these rhabdophane solids is reflected on the dopant level as the presence of several

incorporated curium species within the solid matrix. How this incorporation occurs upon slow dissolution of monazite and recrystallization of rhabdophane under repository conditions, i.e. whether or not this complexity of site types is prevailed should be investigated in future studies to gain further understanding on the performance of monazite host phases for HLW streams. Moreover, detailed structural studies both on pure hydrated actinide phosphates and actinide-bearing lanthanide phosphate solid solutions with higher actinide content are needed for computational predictions of the long-term behavior of monazite waste forms under repository conditions.

## **Notes**

The authors declare no competing financial interest.

## **Acknowledgments**

This work was supported by the German Federal Ministry of Education and Research (BMBF), Project number 02NUK021 and the Excellence Initiative of the German federal and state governments and the Jülich Aachen Research Alliance High-Performance Computing. The authors would like to thank Dr. Martina Klinkenberg for SEM-EDX measurements and PD Dr. Helmut Schlenz for XRD measurements. We thank the JARA-HPC awarding body for time on the RWTH computing cluster awarded through JARA-HPC Partition.

## 5 References

- (1) Meldrum, A.; Boatner, L. A.; Weber, W. J.; Ewing, R. C. Radiation damage in zircon and monazite. *Geochim. Cosmochim. Acta* **1998**, *62*, 2509–2520.
- (2) Meldrum, A.; Boatner, L. A.; Ewing, R. C. A comparison of radiation effects in crystalline  $\text{ABO}_4$ -type phosphates and silicates. *Mineral. Mag.* **2000**, *64*, 185–194.
- (3) Ewing, R. C.; Wang, L. Phosphates as nuclear waste forms, *Rev. Mineral. Geochem.* **2002**, *48*, 673–699.
- (4) Clavier, N.; Podor, R.; Dacheux, N. Crystal chemistry of the monazite structure. *J. Eur. Ceram. Soc.* **2011**, *31*, 941–976.
- (5) Dacheux, N.; Clavier, N.; Podor, R. Versatile Monazite: Resolving geological records and solving challenges in materials science. Monazite as a promising long-term radioactive waste matrix: Benefits of high-structural flexibility and chemical durability. *Am. Mineral.* **2013**, *98*, 833–847.
- (6) Neumeier, S.; Arinicheva, Y.; Ji, Y.; Heuser, J. M.; Kowalski, P. M.; Kegler, P.; Schlenz, H.; Bosbach, D.; Deissmann, G. New insight into phosphate based materials for the immobilisation of safety relevant radionuclides. *Radiochim. Acta* **2017**, *105*, 961–984.
- (7) Oelkers, E. H.; Poitrasson, F. An experimental study of the dissolution stoichiometry and rates of a natural monazite as a function of temperature from 50 to 230 °C and pH from 1.5 to 10. *Chem. Geol.* **2002**, *191*, 73–87.

- (8) Poitrasson, F.; Oelkers, E.; Schott, J.; Montel, J. -M. Experimental determination of synthetic  $\text{NdPO}_4$  monazite end-member solubility in water from 21°C to 300°C: Implications for rare earth element mobility in crustal fluids. *Geochim. Cosmochim. Acta* **2004**, 68, 2207–2221.
- (9) Donald, I. W.; Metcalfe, B. L.; Taylor, R. N. J. The immobilization of high level radioactive wastes using ceramics and glasses. *J. Mater. Sci.* **1997**, 32, 5851–5887.
- (10) Ewing, R. C. Nuclear waste forms for actinides. *Proc. Natl. Acad. Sci. USA* **1999**, 96, 3432–3439.
- (11) Burakov, B. E.; Yagovkina, M. A.; Zamoryanskaya, M. V.; Petrova, M. A.; Domracheva, Y. V.; Kolesnikova, E. V.; Nikolaeva, L. D.; Garbuzov, V. M.; Kitsay, A. A.; Zirlin, V. A. In *Minerals as Advanced Materials*; Krivovichev, S. V., Eds.; Springer, Berlin, Heidelberg, 2008; pp 209–217.
- (12) Popa, K.; Colineau, E.; Wastin, F.; Konings, R. J. M. The low-temperature heat capacity of  $(\text{Pu}_{0.1}\text{La}_{0.9})\text{PO}_4$ . *Solid State Commun.* **2007**, 144, 74–77.
- (13) Terra, O.; Dacheux, N.; Audubert, F.; Podor, R. Preparation and characterization of lanthanum–gadolinium monazites as ceramics for radioactive waste storage. *J. Nucl. Mater.* **2006**, 352, 224–232.
- (14) Holliday, K.S.; Babelot, C.; Walther, C.; Neumeier, S.; Bosbach, D.; Stumpf, T. Site-selective time resolved laser fluorescence spectroscopy of Eu and Cm doped  $\text{LaPO}_4$ . *Radiochim. Acta* **2012**, 100, 189–195.



- (15) Huittinen, N.; Arinicheva, Y.; Kowalski, P. M.; Vinograd, V. L.; Neumeier, N.; Bosbach, D. Probing structural homogeneity of  $\text{La}_{1-x}\text{Gd}_x\text{PO}_4$  monazite-type solid solutions by combined spectroscopic and computational studies. *J. Nucl. Mater.* **2017**, *486*, 148–157.
- (16) van Emden, B.; Thornber, M. R.; Graham, J.; Lincoln, J: The incorporation of actinides in monazite and xenotime from placer deposits in Western Australia. *Can. Mineral.* **1997**, *35*, 95–104.
- (17) Bregiroux, D.; Belin, R.; Valenza, P.; Audubert, F.; Bernache-Assollant, D. Plutonium and americium monazite materials: Solid state synthesis and X-ray diffraction study. *J. Nucl. Mater.* **2007**, *366*, 52–57.
- (18) Konings, R. J. M.; Walter, M.; Popa, K. Excess properties of the  $(\text{Ln}_{2-2x}\text{Ca}_x\text{Th}_x)(\text{PO}_4)_2$  ( $\text{Ln} = \text{La}, \text{Ce}$ ) solid solutions. *J. Chem. Thermodyn.* **2008**, *40*, 1305–1308.
- (19) Raison, P. E.; Jardin, R.; Bouëxière, D.; Konings, R. J. M.; Geisler, T.; Pavel, C. C.; Rebizant, J.; Popa, K. Structural investigation of the synthetic  $\text{CaAn}(\text{PO}_4)_2$  ( $\text{An} = \text{Th}$  and  $\text{Np}$ ) cheralite-like phosphates. *Phys. Chem. Miner.* **2008**, *35*, 603–609.
- (20) Gramaccioli, C. M.; Segalstad, T.V. A uranium- and thorium-rich monazite from a south-alpine pegmatite at Piona, Italy. *Am. Mineral.* **1978**, *63*, 757–761.
- (21) Du Fou de Kerdaniel, E.; Clavier, N.; Dacheux, N.; Terra, O.; Podor, R. Actinide solubility-controlling phases during the dissolution of phosphate ceramics. *J. Nucl. Mater.* **2007**, *362*, 451–458.

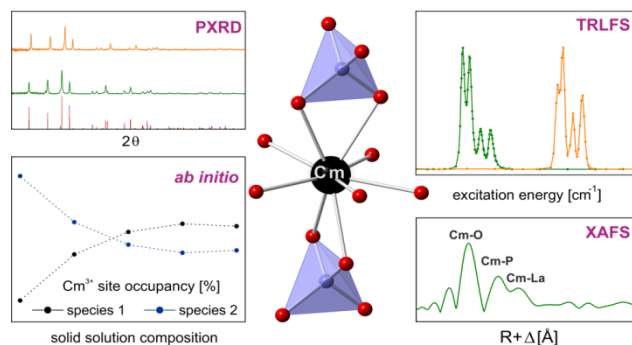
- (22) Cetiner, Z. S.; Wood, S. A.; Gammons, C. H. The aqueous geochemistry of the rare earth elements. Part XIV. The solubility of rare earth element phosphates from 23 to 150 °C. *Chem. Geol.* **2005**, *217*, 147–169.
- (23) Clavier, N.; Dacheux, N. Synthesis, sintering, and leaching of  $\beta$ -TUPD/monazite radwaste matrices. *Inorg. Chem.* **2006**, *45*, 220–229.
- (24) Brandt, F.; Neumeier, S.; Schuppik, T.; Arinicheva, Y.; Bukaemskiy, A.; Modolo, G.; Bosbach, D. Conditioning of minor actinides in lanthanum monazite ceramics: A surrogate study with europium. *Prog. Nucl. Energy* **2014**, *72*, 140–143.
- (25) Li, Y.; Kowalski, P. M.; Blanca-Romero, A.; Vinograd, V. L.; Bosbach, D. Ab initio calculation of excess properties of  $\text{La}_{1-x}(\text{Ln},\text{An})_x\text{PO}_4$  solid solutions. *J. Solid State Chem.* **2014**, *220*, 137–141.
- (26) Rai, D.; Felmy, A. R.; Fulton, R. W. Solubility and ion activity product of  $\text{AmPO}_4 \cdot \text{H}_2\text{O}$  (am). *Radiochim. Acta* **1992**, *56*, 7–14.
- (27) Weigel, F.; Kohl, R. In *Americium and Curium Chemistry and Technology. Topics in f-Element Chemistry, Vol 1*; Edelstein, N. M., Navratil, J. D., Schulz, W.W., Eds.; Springer, Dordrecht, 1985; pp 159–191.
- (28) Buck, E. C.; Moore, D. A.; Czerwinski, K. R.; Conradson, S. D.; Batuk, O. N.; Felmy, A. R. Nature of nano-sized plutonium particles in soils at the Hanford Site. *Radiochim. Acta* **2014**, *102*, 1059–1068.

- (29) Mesbah, A.; Clavier, N.; Elkaim, E.; Gausse, C.; Kacem, I. B.; Szenknect, S.; Dacheux, N. Monoclinic form of the rhabdophane compounds:  $\text{REEPO}_4 \cdot 0.667\text{H}_2\text{O}$ . *Cryst. Growth Des.* **2014**, *14*, 5090–5098.
- (30) Mesbah, A.; Clavier, N.; Elkaim, E.; Szenknect, S.; Dacheux, N. In pursuit of the rhabdophane crystal structure: from the hydrated monoclinic  $\text{LnPO}_4 \cdot 0.667\text{H}_2\text{O}$  to the hexagonal  $\text{LnPO}_4$  (Ln = Nd, Sm, Gd, Eu and Dy). *J. Solid State Chem.* **2017**, *249*, 221–227.
- (31) Shannon, R. D. Revised Effective Ionic Radii and Systematic Studies of Interatomic Distances in Halides and Chalcogenides. *Acta Cryst.* **A32** (1976) 751–767.
- (32) David, F. H.; Vokhmin, V. Thermodynamic properties of some tri- and tetravalent actinide aquo ions. *New J. Chem.* **2003**, *27*, 1627–1632.
- (33) Edelstein, N. M.; Klenze, R.; Fanghänel, T.; Hubert, S. Optical properties of Cm(III) in crystals and solutions and their application to Cm(III) speciation. *Coord. Chem. Rev.* **2006**, *250*, 948–973.
- (34) Kimura, T.; Choppin, G. R. Luminescence study on determination of the hydration number of Cm(III). *J. Alloys Compd.* **1994**, *213-214*, 313–317.
- (35) Holliday, K.; Finkeldei, S.; Neumeier, S.; Walther, C.; Bosbach, D.; Stumpf, T. TRLFS of  $\text{Eu}^{3+}$  and  $\text{Cm}^{3+}$  doped  $\text{La}_2\text{Zr}_2\text{O}_7$ : A comparison of defect fluorite to pyrochlore structures. *J. Nucl. Mater.* **2013**, *433*, 479–485.
- (36) Schmidt, M.; Stumpf, T.; Walther, C.; Geckeis, H.; Fanghänel, T. Phase transformation in  $\text{CaCO}_3$  polymorphs: A spectroscopic, microscopic and diffraction study. *J. Colloid Interface Sci.* **2010**, *351*, 50–56.

- (37) Schmidt, M.; Stumpf, T.; Marques Fernandes, M.; Walther, C.; Fanghänel, T. Charge compensation in solid solutions. *Angew. Chem. Int. Ed.* **2008**, *47*, 5846–5850.
- (38) Webb, S. M. SIXpack: a graphical user interface for XAS analysis using IFEFFIT. *Phys. Scr.* **2005**, *T115*, 1011–1014.
- (39) Ressler, T. WinXAS: a program for x-ray absorption spectroscopy data analysis under MS-windows. *J. Synchr. Rad.* **1998**, *5*, 118–122.
- (40) Ankudinov, A. L.; Ravel, B.; Rehr, J.; Conradson, S. D. Real-space multiple-scattering calculation and interpretation of x-ray-absorption near-edge structure. *Phys. Rev. B* **1998**, *58*, 7565–7576.
- (41) Giannozzi, P.; Baroni, S.; Bonini, N.; Calandra, M.; Car, R.; Cavazzoni, C. et al. QUANTUM ESPRESSO: a modular and open-source software project for quantum simulations of materials. *J. Phys. Condens. Matter* **2009**, *21*, 395502.
- (42) Methfessel, M.; Paxton, A. T. High-precision sampling for Brillouin-zone integration in metals. *Phys. Rev. B* **1989**, *40*, 3616–3621.
- (43) Zunger, A.; Wei, S. -H.; Ferreira, L. G.; Bernard, J. E. Special quasirandom structures. *Phys. Rev. Lett.* **1990**, *65*, 353–356.
- (44) Blanca-Romero, A.; Kowalski, P. M.; Beridze, G.; Schlenz, H.; Bosbach, D. Performance of DFT plus U method for prediction of structural and thermodynamic parameters of monazite-type ceramics. *J. Comput. Chem.* **2014**, *35*, 1339–1346.
- (45) Beridze, G.; Birnie, A.; Koniski, S.; Ji, Y.; Kowalski, P. M. DFT plus U as a reliable method for efficient ab initio calculations of nuclear materials. *Prog. Nucl. Energ.* **2016**, *92*, 142–146.

- (46) Ni, Y.; Hughes, J. M.; Mariano, A. N. Crystal chemistry of the monazite and xenotime structures. *Am. Mineral.* **1995**, *80*, 21–26.
- (47) Ochiai, A.; Utsunomiya, S. Crystal chemistry and stability of hydrated rare-earth phosphates formed at room temperature. *Minerals* **2017**, *7*, No. 84.
- (48) Huittinen, N. Sorption of trivalent actinides onto gibbsite,  $\gamma$ -alumina, and kaolinite - A spectroscopic study of An(III) interactions at the mineral-water interfaces. Ph.D. Thesis, University of Helsinki, Finland, 2013.
- (49) Holliday, K.; Handley-Sidhu, S.; Dardenne, K.; Renshaw, J.; Macaskie, L.; Walther, C.; Stumpf, T. A new incorporation mechanism for trivalent actinides into bioapatite: A TRLFS and EXAFS study. *Langmuir* **2012**, *28*, 3845–3851.
- (50) Huittinen, N.; Arinicheva, Y.; Schmidt, M.; Neumeier, S.; Stumpf, T. Using  $\text{Eu}^{3+}$  as an atomic probe to investigate the local environment in  $\text{LaPO}_4$ - $\text{GdPO}_4$  monazite end-members. *J. Colloid Interface Sci.* **2016**, *483*, 139–145.
- (51) Arinicheva, Y.; Popa, K.; Scheinost, A. C.; Rossberg, A.; Dieste-Blanco, O.; Raison, P.; Cambriani, A.; Somers, J.; Bosbach, D.; Neumeier, S. Structural investigations of  $(\text{La,Pu})\text{PO}_4$  monazite solid solutions: XRD and XAFS study. *J. Nucl. Mater.* **2017**, *493*, 404–411.
- (52) Assaaoudi, H.; Ennaciri, A.; Rulmont, A.; Harcharras, M. Gadolinium orthophosphate weinschenkite type and phase change in rare earth orthophosphates. *Phase Transitions.* **2000**, *12*, 1–13.

## For Table of Contents Only



## TOC synopsis

This study combines spectroscopic and computational investigations to understand the incorporation of curium ( $\text{Cm}^{3+}$ ) in rhabdophane and monazite solid solutions. In monazites,  $\text{Cm}^{3+}$  incorporation occurs on one specific lattice site. The local order around the dopant in these monazites is dependent on the solid solution composition. La-rich hydrated rhabdophane solid solutions show preferential incorporation of  $\text{Cm}^{3+}$  on non-hydrated lattice sites, despite the prevalence of cation sites associated with water of hydration in the rhabdophane structure.